




## Decoupling of dust cloud and embedding plasma for high electron depletion in nanodusty plasmas

Andreas Petersen<sup>1</sup><sup>✉</sup>, Oguz Han Asnaz<sup>1</sup>, Benjamin Tadsen<sup>1</sup><sup>1</sup> & Franko Greiner<sup>1,2</sup><sup>✉</sup>

In recent years nanoparticles have become key technological products, e.g., as coatings with tunable optical gap in third generation solar cells, as nanocrystals for photonic applications, and as pharmaceutical nanocarriers. In particle sources, that use reactive, nanodusty plasmas, a high dust density changes the properties of the dusty plasma compared to a dust free plasma considerably, as electron depletion leads to a reduced number of free electrons. This is called the Havnes effect and was central for the understanding of the famous spokes in Saturns rings. We see here, that it is also important for technological applications. Using self excited dust density waves (DDW) as a diagnostic tool, we completely characterize an argon discharge with embedded amorphous hydrocarbon nanoparticles of different size and density. The results show, that electron depletion governs the charge of dust grains, while the size of the particles has only a weak influence. The ion density and electric potential profile are almost independent of both, dust size as well as dust density. This suggests, that the rf generated plasma and the dust cloud seem to coexist and coupling of both is weak.

<sup>1</sup>Institute of Experimental and Applied Physics, Kiel, Germany. <sup>2</sup>Kiel Nano, Surface and Interface Science KiNSIS, Kiel University, Kiel, Germany.  
<sup>✉</sup>email: [apetersen@physik.uni-kiel.de](mailto:apetersen@physik.uni-kiel.de); [greiner@physik.uni-kiel.de](mailto:greiner@physik.uni-kiel.de)

In the mid eighties of the last century, plasma assisted chip production suffered from drop outs due to generated dust particles. This dilemma was the spark, which established the new research field of (nano)dusty plasmas. While it was first presumed that the particles were sputtered from the source wafers, the surprising result was that nanoparticles can grow inside of a discharge from molecular precursors<sup>1</sup>.

Recently, the field has seen a paradigm shift, as plasma created nanoparticles have become a valuable product, and research focuses more on the generation processes and properties of the particles themselves.

Under the non-equilibrium conditions of low pressure plasmas<sup>2</sup>, with relatively high electron energies (around 50,000 K or 4 eV) and ions as well as neutrals at room temperature, chemical reactions are possible, which can not be observed in classical wet chemistry. Reactive, particle producing plasmas, often noble gas plasmas with an admixture of silane<sup>3</sup>, acetylene<sup>4</sup> or methane<sup>5</sup>, are central for a wide range of technological applications.

Their use in the technical field ranges from coatings to prime surfaces, for surface protection, for optical purposes<sup>6–8</sup>, and even to provide tailored nano dots in solar cell coatings<sup>9,10</sup>. In the medical field however, nanoparticles have become relevant as drug carriers<sup>11,12</sup>. They are a key feature to stabilize mRNA during application<sup>13</sup>. And in recent developments nanoparticles are even considered to deliver drugs into the pulmonary system to treat SARS-CoV2<sup>14</sup>.

Several aspects of the creation of dust particles in a plasma have been thoroughly explored: The plasma chemical reactions<sup>15</sup> which lead to free radicals and their polymerization into clusters<sup>16</sup>, the importance of trapped, negatively charged precursors<sup>17</sup> and lastly different phases of the growth mechanism<sup>18,19</sup>.

While there are comprehensive approaches to model interaction of all components of a nanodusty plasma<sup>20,21</sup>, the basic physics of the nanodusty plasmas, which are mandatory to understand the processes in reactive plasmas, is largely unexplored. A detailed knowledge of the charging, an understanding of the confinement of nanoparticles, and changes of the plasma parameters are keys to systematically advance production processes and to learn about synergistic effects.

Support for the understanding of dusty plasmas at high dust densities comes from a completely different side, from astrophysics. The observation of spokes in the rings of Saturn by the passing Voyager 1 and Voyager 2 satellites in 1979/1980 was one of the trigger events for the new field of physics of dusty plasma. To explain the sporadic appearance and disappearance of the spokes, Goertz and Morfill<sup>22</sup> proposed a model, which is based on meteor impacts on the ring, producing plasma densities high enough to levitate negatively charged, micron sized ice particles. Havnes showed that the created plasmas have high dust density<sup>23</sup>. This results in a depletion of electrons and leads to a reduced dust charge<sup>24</sup>.

The key equation to describe the condition of a plasma containing a high dust density is the quasi neutrality equation

$$n_i - (n_e + Zn_d) = 0. \quad (1)$$

In the following, we restrict ourselves to a three component plasma of argon ions with a single positive charge  $e$  and density  $n_i$ , dust particles with a negative charge of  $Z$  elementary charges and density  $n_d$ , as well as electrons with density  $n_e$ . As seen from Eq. (1), a high density of dust particles leads to a depletion of electrons. The  $n_e + Zn_d$  term in Eq. (1) creates the negative charge which has to balance the positive ion charge. This means, that a high negative charge  $Ze$  of the dust particles effectively reduces

the number of free plasma electrons, leading to an electron depleted plasma.

Havnes et al.<sup>25</sup> introduced a dimensionless order parameter which describes the depletion of electrons, today called Havnes parameter

$$P = 4\pi\epsilon_0 a \frac{k_B T n_d}{e^2 n_i}, \quad (2)$$

with  $a$  the particles radius,  $T$  temperature,  $\epsilon_0$  vacuum permittivity, and  $k_B$  the Boltzmann factor. Figure 1 gives an intuitive picture of the potential in a plasma when the dust density is increased at constant  $a$  and  $T$ . For  $P < 1$  a “dust in plasma” situation is found. The particles are screened by the surrounding electrons and ions and they charge up to their maximum negative value, leading to deep potential wells. Between these wells the electrical potential  $\Phi$  recovers to the plasma potential  $\Phi_p$  of the pristine, dust free plasma. The situation changes when  $P \approx 1$ , the potential wells of the particles start to overlap and the dusty plasma creates its own “cloud plasma potential”  $\Phi_c$  which is lower than that of the dust free plasma. For even higher Havnes parameter  $P \gg 1$ , the potential wells are vanishing. The dust particles are on the same potential, this is the regime of electron depletion.

When using a spherical capacitor model, the particle charge  $q_d$  is determined by:

$$q_d = 4\pi\epsilon_0 a (\Phi_f - \Phi_c), \quad (3)$$

which is the solution for the collision-less orbital motion limited (OML)<sup>26</sup> charging. This is the dust charging model, we will use. There are approaches that take collisions into account, however the applicability at pressures lower than 30 Pa or with considerable electron depletion is questionable<sup>27</sup>.

In the astrophysical situation modeling the electron depleted plasma is based on the assumption, that this plasma is embedded in a dust free plasma which can deliver additional ions needed to account for the dust charging<sup>24</sup>. In Goertz et al.<sup>28</sup> this model was named “Boltzmann distributed ion model” (BIM), as its main assumption is, that the ions inside of the dust cloud are provided by an undisturbed surrounding plasma and are Boltzmann distributed. For a low pressure rf plasma the BIM model can not be used, as there is no surrounding plasma to deliver said ions. Instead the ions are produced by ionizing collisions with electrons inside of the dusty plasma. The model suggested by Melzer and Goree<sup>29</sup> takes this internal ion source into account leading to a constant ion density model (CIM)<sup>28</sup>.

Already in 1994 Barkan could verify the existence of the Havnes effect in a Q machine plasma<sup>30</sup>. In 2011 Goertz et al. performed a comparative study in a large, thermionic magnetic box plasma and could show that the Havnes effect is observable and can be described with BIM and CIM in such a plasma<sup>28</sup>. However, both experiments used a setup, where micron sized

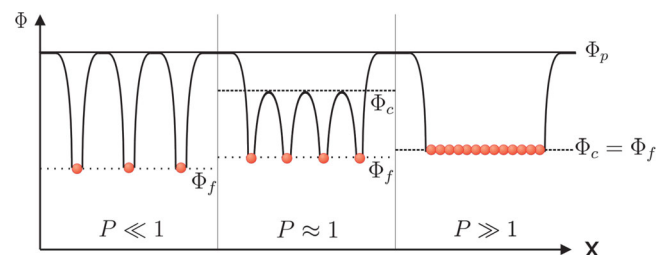


**Fig. 1 Different regimes dependent on the Havnes Parameter.** Effect of the dust density on the potential  $\Phi$  of a dusty plasma, when the Havnes parameter  $P$  is increased. The plasma potential of the dust free plasma is  $\Phi_p$ , the floating potential of dust grains  $\Phi_f$ , and the plasma potential in a dense cloud is  $\Phi_c$ . Adaption from Goertz<sup>24</sup>.

dust was falling through a plasma, i.e., the experimental situation was not fully stationary.

Until 2015 no experiment existed, that could create and characterize a stationary high density dust cloud in an argon plasma. Two achievements made this possible. The first one was the use of sub-micron particles. For sub-micron particles gravity is only a minor force and the particles can fill the whole plasma volume and form a 3D dust cloud. The second achievement was to use a reactive argon acetylene plasma as the particle source. The plasma chemistry in an argon acetylene plasma provides reactive components as precursors, which polymerize and grow to become spherical and mono disperse particles<sup>3,4,31</sup>. Using light scattering methods, the particle size and refractive index<sup>32–34</sup> can be determined, as well as the local particle density by laser light extinction (a cross section of the dust cloud can be seen in Fig. 2). Recording the evolution of self excited dust density waves (DDW) and fitting a model description of such waves to the experimental data<sup>35–37</sup> allows us to fully characterize the three component plasma. We find, that the plasma generation process is almost independent of particle size and density for the explored regime. We also determine, that depletion of electrons from the discharge onto the dust is important and mainly determines the dust charge.

## Results

**Procedure.** For the experimental campaign presented here, we created a dusty plasma with particle radii of 120–160 nm, which is an increase of 230% in mass. All discharge parameters are kept constant (base pressure 21 Pa, rf power 8 W).

To achieve the desired three component plasma consisting only of electrons, argon ions and dust particles, the admixture of acetylene to the feed gas is introduced into the discharge and the resulting plasma chemistry leads to particle growth. When the desired size is reached, the acetylene flow is stopped and any hydrocarbon remnants are quickly consumed or flushed from the system.

Figure 2 shows a dust cloud created with this process. The cylindrical cloud is illuminated by a laser stripe (laser L1 (640.3 nm) as shown in the setup). The scattered laser light creates a 2D image of the cylindrical cloud. At the top and bottom a reflection can be seen on the surface of the electrodes. The cloud shows the characteristic dust free region in the center named 'void' and self-excited dust density waves (DDW). The dust density in such a cloud is typically  $1 \times 10^{13} \text{ m}^{-3}$  at an ion density of  $1 \times 10^{15} \text{ m}^{-3}$  leading to a Havnes parameter of  $P = 10 \dots 50$ <sup>37</sup>. This results in a drastic electron depletion with a dust charge of only 10...50 elementary charges. In comparison, a single dust

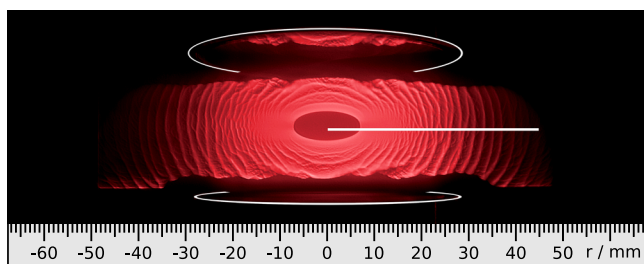


**Fig. 2 Light scattering image of nanodust cloud.** A 2D image of the scattered light of a laser stripe going from right to left through the center of a discharge chamber. On top and bottom the rf driven electrodes with a diameter of 58 mm are highlighted. Using a short exposure time of 0.8 ms reveals the existence of self excited dust density waves. The region of the dust density wave diagnostic in the middle is also marked.

particle of 190 nm radius and  $P \ll 1$  would gain up to 1600 elementary charges under assumption of OML.

To measure the dust density via laser light extinction, the optical properties of the dust particles need to be known. These are determined by means of kinetic Mie polarimetry<sup>32–34</sup> using the rotating compensator polarimeter shown in the setup. The diagnostic of dust charge, ion density, and electric field uses an analysis method that is based on the dispersion relation of the DDW<sup>35–37</sup>. From the wave data recorded by the camera C4, local frequencies and wavenumbers can be calculated, using a Hilbert transform approach. A fitting procedure using the dispersion relation of the DDW gives estimates of dust charge, ion density, and electric field<sup>37</sup>. The modeling takes into account electron depletion and the resulting decrease of particle charge using CIM. Although CIM assumes a constant ion density, the local analysis at each radial position leads to spatially changing ion density, as the wave changes its frequency and wavenumber when it moves through the inhomogeneous plasma (Fig. 2).

For the five radii the full data of extinction, polarimetry and DDW videos is acquired and analysed by the presented methods<sup>34,37,38</sup>. Afterwards the discharge is extinguished and the process repeated for a new target radius. This ensures high consistency.

With the fast camera C4 (as shown in the setup) videos of the dust density wave are taken at 4000 fps containing 1k consecutive frames. As an example, Fig. 3a shows data obtained from one frame of the video for a particle size of 139 nm. Below a vertical average of the image shows the amplitude of the DDW. The red box marks the region used for Fourier analysis and the vertical dashed line at 30 mm marks the rim of the shielded electrode. Figure 3(b) shows the instantaneous frequencies and wavenumbers ( $\omega(r)$ ,  $k(r)$ ) determined by Hilbert transform. These ( $\omega(r)$ ,  $k(r)$ ) data sets and the radial dust density profiles are the input

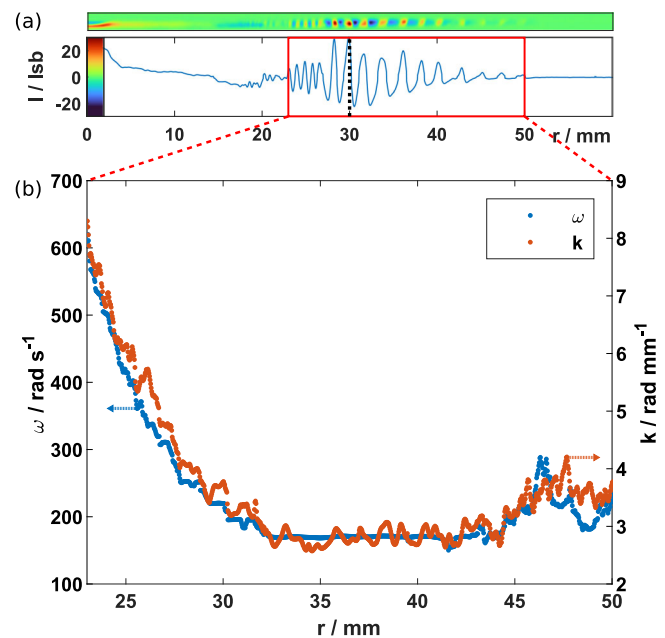


**Fig. 3 Analysis of 4k fps video for dust density wave diagnostic.** **a** A 60 mm long and 3 mm high image of the wave patterns acquired with Camera C4. It shows the fluctuations by subtracting the mean intensity over all frames from a single frame. The graph below this image shows the column average in units of camera's least significant bit. The dashed black line denotes the extent of the electrodes shield. Analysis for **(b)** is confined to the red box. **b** Local  $\omega$  and  $k$  of the dust density wave determined by means of Hilbert transform.

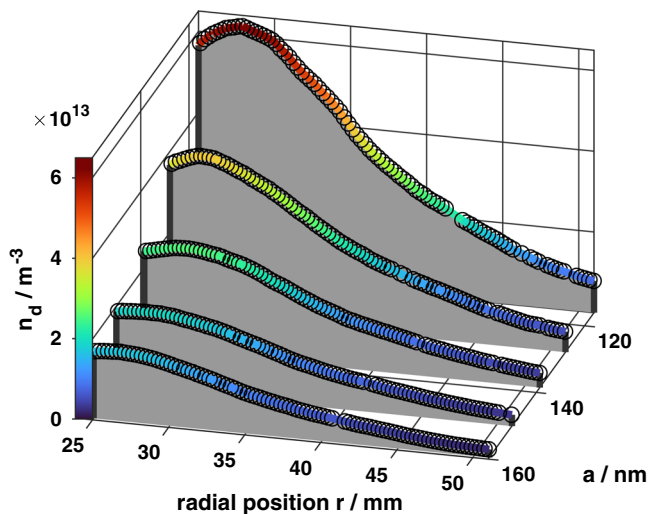


**Fig. 4** Radial dust density  $n_d(r)$ . The shape of the dust density profile  $n_d(r)$  is very similar for the different particle radii. As the dust particles grow, the overall density decreases, because of losses from the discharge. The color scheme supports visual comparability, the particle radius is  $a$  and the radial position  $r$ .

data for the so called “Dust density wave diagnostic” (DDW-D) which is described in detail by Tadsen<sup>37</sup>. The DDW-D is performed for all particle radii. The dust density waves show a linear, i.e., acoustic dispersion, similar to previous results<sup>37,39</sup>.

In Fig. 4 the radial dust density profiles are presented, which were measured by means of the extinction setup (Laser stripe L1 and cameras C1, C2, C3, see detailed explanation in Methods—Diagnostic for dust density and particle size). Due to the fact, that the creation of larger particles needs more time and the confinement of the dust inside of the plasma is not perfect (see Fig. 9 of Tadsen<sup>40</sup>), the total density of the dust is decreased for large dust particles.

**Decoupling.** To match our kinetic three particle model of a homogeneous, infinite plasma to a measured data set  $(\omega, k)_{ex}$ , the models dispersion relation is evaluated for its most unstable mode  $(\omega, k)_m$ . It is assumed, that this mode, exhibiting the highest growth rate, will be observed in the experiment. Evaluation is done separately at each radial position. In Methods—Dust density wave diagnostic, the additional input data needed to do the data analysis is given. Figure 5 presents the results of the DDW-D for different particle radii. Figure 5a shows the ion density profile. It can be seen, that the dust density (Fig. 4) and dust size both change significantly, while the ion density does not change. This is a really surprising finding, as it means, that the ion production rate seems to be unaffected. The plasma production, which mainly bases on the generation of argon ions by means of inelastic collisions of electrons with neutral argon atoms, remains untouched. In addition, an observation of Klindworth<sup>41</sup> could be verified. The radial density profile of a dusty plasma with considerable dust density is convex, in contrast to the density profile in a pristine argon plasma, which is concave.

**Electron depletion.** Figure 5b shows the severe effect of electron depletion. The electron density lies more than a factor of hundred below the ion density, as the dust particles snatch away nearly all free electrons. As a detail, an increase of the electron density is seen for the largest dust particles (160 nm) at larger radial position, far out of the electrodes. Here, the dust density becomes very small and consequently, the electron density starts to increase.

The plasma potential is one of the plasma parameters, that determines the dust density profile, as it provides the electric forces which lead to the confinement of the nanoparticles in the discharge. As the DDW-D determines the radial electric field, the potential  $\phi(r) = \int E dr + \phi_0$  can only be determined with respect to a reference point, which we set  $\phi_0 = \phi(52 \text{ mm}) = 0$  volt for all particle radii. The result is a nearly linear drop of the plasma potential  $\phi(r)$ . This corresponds to the finding of Tadsen<sup>37</sup>, as well as to probe measurements in the pristine argon plasma.

Similar to the ion density, the plasma potential shows no variation with the change of the dust radius and the dust density, Fig. 5c.

**Dust charge.** The dependency of the dust charge on the radial position can be seen in Fig. 5d. The dust charge is extremely small in comparison to a single dust particle in a pristine argon plasma. There are no pronounced radial features for the different particle radii. However, an overall increase of the dust charge is seen for increasing particle size. This increase is correlated with the decrease of the dust density (Fig. 4), as a higher dust density results in a higher electron depletion at constant ion density.

The effect of the dust, i.e., the effect of its size and its density on the dusty plasma is expressed by the Havnes parameter  $P(a, n_d, n_p, T_e)$  (Eq. (2)). It is no surprise, that  $P$  is radially dependent, see Fig. 6. For all particle sizes  $P \gg 1$  is valid, the plasma is in a strongly electron depleted state. Again, only a small region radially outside of the electrode shows a smaller Havnes parameter of  $P \approx 10$ , as the dust density at the highest dust radius is lower at this distance (lower right corner in Fig. 6).

## Conclusions

An argon plasma was created at constant rf power of 8 W, containing a nanodust cloud at high dust density (high Havnes parameter). The presented data shows, that the plasma’s radial density and potential profile remain unchanged when the dust size is varied from 117 to 158 nm, while the dust density is changed from  $6 \times 10^{13} \text{ m}^{-3}$  to  $1.8 \times 10^{13} \text{ m}^{-3}$ . This suggests, that the plasma production by means of ionising collisions of energetic electrons with the argon background, and the dust cloud coexist and are not strongly coupled to each other. The electron depletion determines the specific dust charge at a given dust density. The Havnes parameter provides a direct measure of said depletion. The new findings are supported by a Langmuir probe study of Bilik et al.<sup>42</sup>, which was done in a reactive silan-argon plasma, containing dust. The Havnes parameter of the data presented in ref. <sup>42</sup> can be determined using Eq. (2) and is around  $P = 2$ , i.e.,  $P$  is much smaller than in our experiments. Nevertheless the electron depletion is significant and the results are therefore relevant in comparison to the presented results. Bilik et al. observed that the electron energy probability function (EPPF) changes significantly, when dust is present in the plasma. It changes from a Druyvesteyn function to a Maxwellian, leading to a pronounced increase of the “Maxwell tail” of high energy electrons, responsible for the ionisation. The Maxwell tail doesn’t change its shape, when the particles grow over time from 25 to 150 nm. This observation perfectly matches our finding, that the background plasma remains unchanged for different dust sizes and dust densities, and can explain, that the ion sources inside of the plasma remain unchanged during the growth process. The result of Bilik et al. were underpinned by kinetic modeling of Denysenko et al.<sup>43</sup>.

## Methods

In this section the experimental setup, the diagnostics and the data analysis methods are presented.



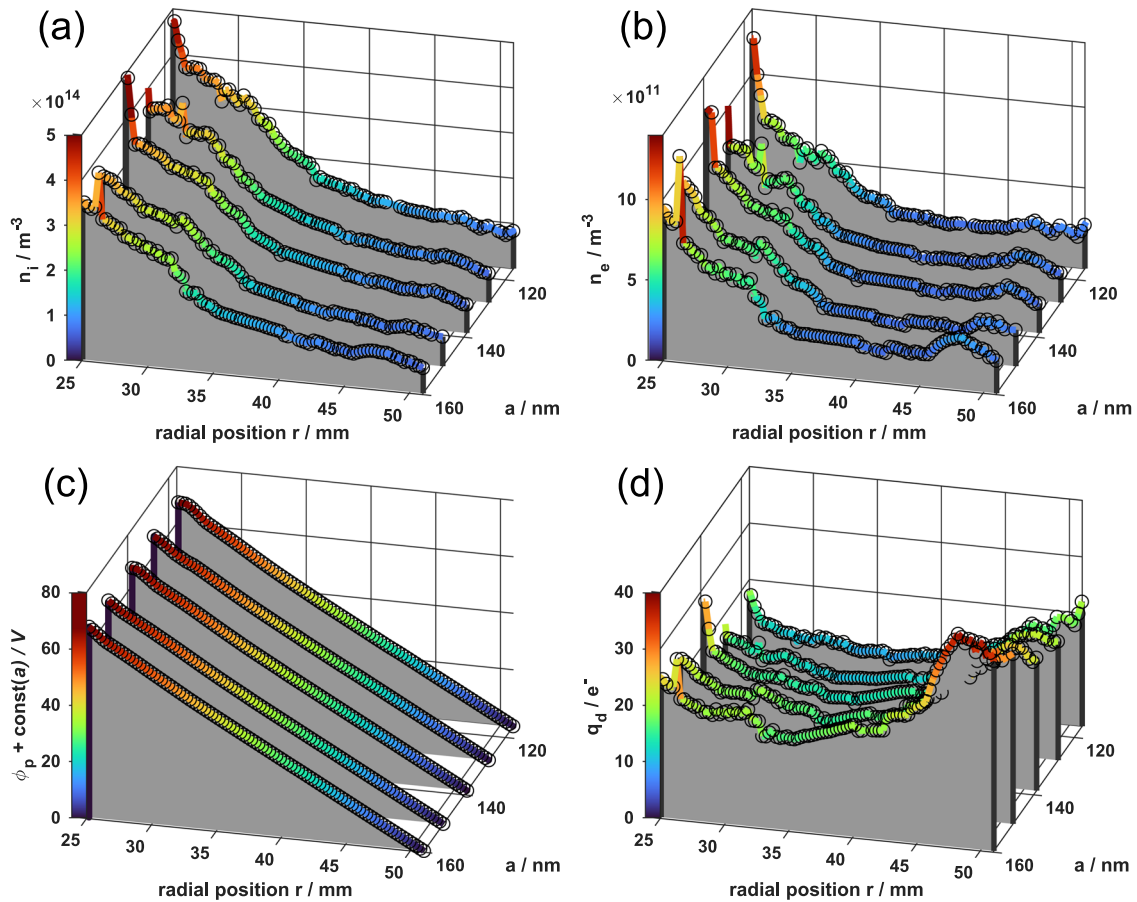


**Fig. 5 Results of the DDW analysis.** Results for different particle radii  $a$  along the radial direction  $r$ : **a** ion density  $n_i(r)$ , **b** electron density  $n_e(r)$ , **c** electric potential (for the discussion of a common reference see Methods—Dust density wave diagnostic), and **d** dust charge  $q_d$ .

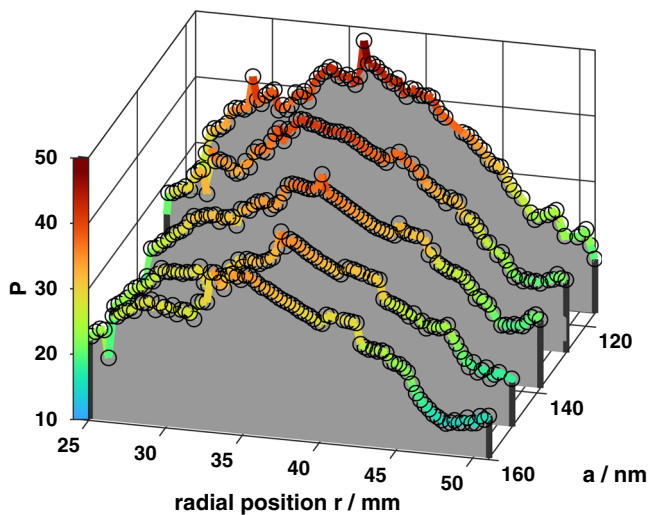


**Fig. 6 Havnes parameter  $P$ .** The Havnes parameter deduced from the dust density wave analysis along the radial direction  $r$  for all particle sizes  $a$ .

**Experimental setup.** The experiments are performed in a parallel plate reactor with cylindrical electrodes of 58 mm diameter and an electrode gap of 30 mm. A side view of the chamber and the rf wiring are shown in Fig. 7. A vertical laser stripe illuminates a 2D cross section of the cylindrically symmetric dust cloud. A camera positioned perpendicular to the laser stripe (out of the paper plane in Fig. 7) can be used to monitor the dust cloud. Figure 2 is an example of a typical dust cloud image made by using a red laser and a fast camera. To start the experiments an argon pressure of 21 Pa is set with a flow controller leading to an argon flow of 8 sccm, the plasma is ignited with a rf power of 8 W and 20%

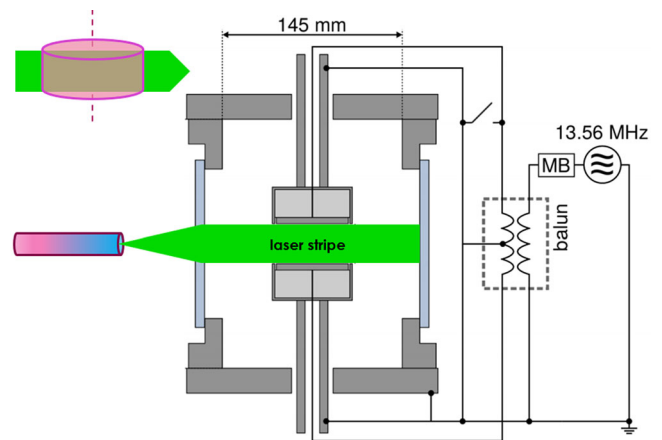


**Fig. 7 Side view of the plasma chamber.** A generator in series with a match box (MB) and balun drives the electrodes with a rf signal of 13.56 MHz. The balun symmetrizes the signal. Gas is fed into the chamber on top and pumped out on the bottom. For simplicity only the vertical, expanded laser stripe is shown (it is laser L1 in the experimental setup). The light scattered from L1 produces an image of a 2D cross section of the cylindrically symmetric dust cloud.

acetylene is added to the argon flow thereby maintaining a constant total gas flow of 8 sccm.

During the experiments, different diagnostics are used to monitor particle size and density. Figure 8 shows a top view of said diagnostics. A rotating compensator polarimeter (RCP) monitors the polarisation state of light scattered by the growing dust particles from the red laser beam at 662.6 nm (laser L2 in Fig. 8). A matching

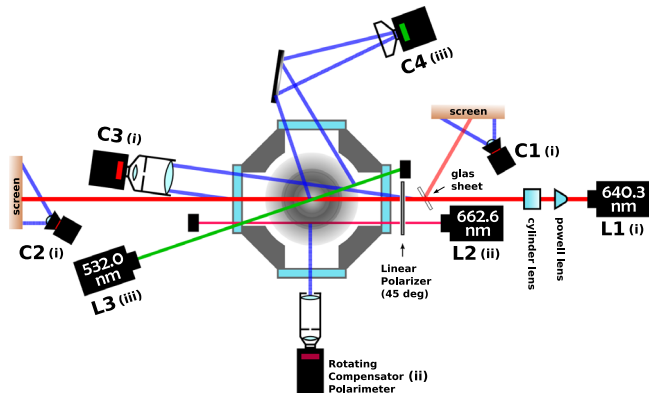


**Fig. 8 Top view of the experimental setup.** Top view of the plasma chamber and all optical diagnostics. Three optical diagnostics are combined. (i) Extinction setup for dust density measurements: Laser L1 (expanded to a vertical stripe) and cameras C1, C2 and C3 (ii) Mie Polarimetry for dust size diagnostic: The scattered light of laser beam L2 is acquired by a rotating compensator polarimeter. (iii) Dust density wave diagnostic: Laser beam L3 and fast camera C4.

band pass filter blocks all other light from reaching the RCP. The vertically expanded red laser L1 (640.3 nm) allows to monitor the dust cloud via camera C3, and is used to perform 1D extinction measurements using the intensity of camera C2 calibrated with the initial intensity measured with camera C1. A horizontal, green Laser beam L3 (532 nm) passes the center of the discharge and videos of the scattered light of laser L3 are taken with the fast camera C4 at appropriate times, to acquire video sequences of the dust density wave. A matching band pass filter in front of camera C4 ensures, that only the scattered light of laser L3 is entering the camera. A single snapshot out of one of these video sequences is shown in Fig. 3a.

As mentioned, the RCP and camera C3 are equipped with filters which block light with a wavelength of 532 nm.

In the following sections the diagnostics for dust size, dust density and nanodusty plasma parameters are described in detail.

**Diagnostic for dust density and particle size.** The dust particles are created using a reactive argon acetylene plasma. Since effective growth rate and onset time can vary, it is important to monitor the particle growth. After adding acetylene to the argon plasma, spherical amorphous hydrogenated carbon particles (a:C-H) start to grow from molecular precursors up to sizes of a few hundred nanometers in radius. By switching off the acetylene admixture, the particle growth stops, and after consumption of the remaining precursors a dusty plasma, consisting only of electrons, ions and (negatively) charged dust remains. To create particles of different sizes, but with identical structural and chemical makeup, the discharge was extinguished after each measurement which removes the particles. The observed growth rate for all cycles was 2.0 nanometer per second. The dust particles are spherically shaped and have a narrow size distribution. The rotating compensator polarimeter (RCP) depicted in Fig. 8 acquires a time series of the polarimetric angles  $\Delta$  and  $\Psi$  as well as the degree of polarisation (*DoP*). This fully characterizes the polarisation state of the scattered light. From this time series the radius of the dust particles is determined by means of kinetic Mie polarimetry<sup>32,33</sup> and is described in detail by Groth<sup>34</sup>. Figure 9a shows the measured  $\Delta(\Psi)$ -curve for a long growth period, the Mie model curve fitted by the algorithm presented in<sup>34</sup>, and  $\Delta$  and  $\Psi$  of the aborted growth processes, that create dusty plasmas with differing particle sizes. The outcome of the fitting procedure are the refractive index of the particles ( $N = 2.05 + i0.07$ ) as well as the radius. The extinction efficiency  $Q_{\text{ext}}$  of the particles, which is a function of refractive index and particle size, is needed to determine the absolute dust density, from a combination of a 1D extinction measurement (cameras C1 and C2 in Fig. 8) and a video that is taken under a shallow angle from the dust cloud evolving over time (camera C3 in Fig. 8, a telecentric lens is used). The detailed procedure is presented by Groth<sup>44</sup>. Assuming cylindrical geometry, which is justified by computed tomography (CT) measurements<sup>45</sup>, the dust density profile can be reconstructed. As an example, Fig. 9b shows the density profile reconstructed for the particle radius  $a = 140$  nm. The radial dust density profiles shown in Fig. 4 and the dust radius provided here are needed as input for the dust density diagnostic, described in the next section.

**Dust density wave diagnostic.** The DDWs are waves in a weakly coupled system, i.e. the dust particles are in a gaseous state where the kinetic dust temperature is high compared to the particle-particle interaction. DDWs are ion-dust streaming instabilities of the Buneman type<sup>46,47</sup>. In the context of dusty plasmas, they were first described in a theory paper of Rao et al.<sup>35</sup>. In 1997 Kortshagen proposed the DDW as a diagnostic for the size of nanometer sized particles<sup>48</sup>. He used a three-

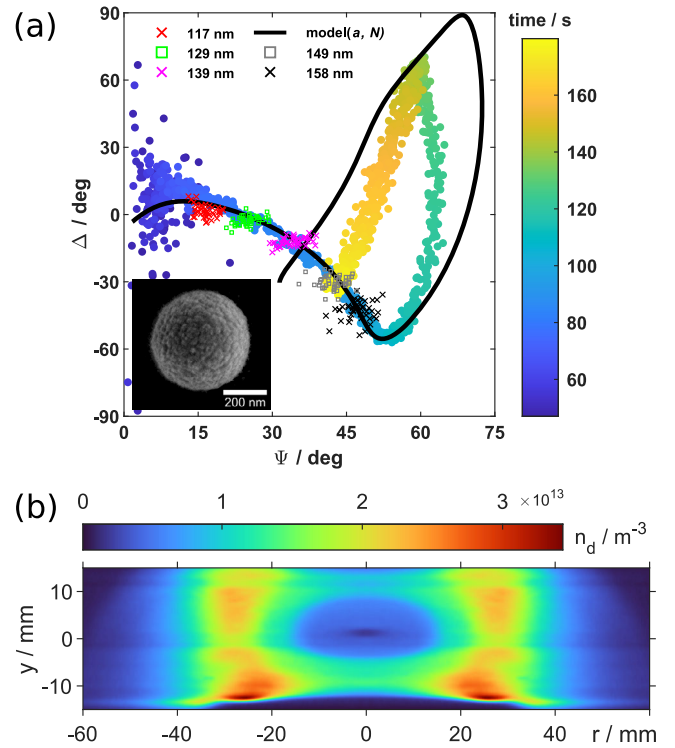


**Fig. 9 Dust particle size and density measurement.** **a** Kinetic  $\Delta(\Psi)$ -Curve (filled circles). The measured values of  $\Delta$  and  $\Psi$  change over time (see colorbar), as the particles size increases. The black curve is the fit of the Mie model. For larger particles a deviation of the model, due to multi-scattering, is expected<sup>34</sup>. The “clouds” of symbols along the curve show the settling of  $\Delta$  and  $\Psi$  values after acetylene admixture was stopped. The inset is the SEM image of a typical a-C:H-particle. **b** Dust density profile for a dust radius of  $a = 140$  nm. A line integrated, vertically resolved extinction measurement and the extinction efficiency  $Q_{\text{ext}}$  from kinetic Mie polarimetry is used to reconstruct the cylindrically symmetric 2D dust density profile  $n_d(r, y)$ .

fluid model for dust, ions and electrons in a homogeneous, infinite plasma, assuming that the phase velocity of the DDW is small compared to the ion and electron thermal velocity. The relatively simple fluid model is applicable to our experimental situation, except that the ions have to be treated kinetically as the ion drift velocity is in the range of a few ion thermal velocities<sup>36</sup>.

For an in depth discussion refer to Ruhunusiri<sup>49</sup>. Considering small perturbations of the wave potential  $\bar{\Phi}$  and the density  $\bar{n}_j$  of species  $j$ , its susceptibility can be written as

$$X_j = -\frac{q_j \bar{n}_j}{\epsilon_0 k^2 \bar{\Phi}}. \quad (4)$$

For the electrons we neglect inertia. For the ions we consider a streaming velocity  $\mathbf{v}_i$  and ion-neutral friction with the collision frequency  $\nu_{\text{in}}$ . For dust particles we take into account a weak compressibility  $\beta = 1/n_d k_B T_d$  due to coupling of particles and a dust neutral friction with collision frequency  $\nu_{\text{dn}}$ . This leads to species dependent susceptibilities

$$X_e = \frac{1}{k^2 \lambda_{\text{De}}^2}, \quad (5)$$

$$X_i = \frac{\omega_{\text{pi}}^2}{k^2 \nu_{\text{Ti}}^2 + \mathbf{k} \cdot \mathbf{v}_i (-\mathbf{k} \cdot \mathbf{v}_i + i\nu_{\text{in}})}, \quad (6)$$

$$X_d = \frac{\omega_{\text{pd}}^2}{k^2 (\beta n_d m_d)^{-1} - \omega (\omega + i\nu_{\text{dn}})}. \quad (7)$$

Here  $k, \omega$  are the wave vector and angular frequency,  $\lambda_{\text{De}}$  the electron Debye length,  $\nu_{\text{Ti}}, \nu_{\text{Td}}$  the thermal speed of ions and dust and  $\omega_{\text{pi}}, \omega_{\text{pd}}$  their plasma frequencies. With this we get to

$$0 = 1 + X_e + X_i + X_d, \quad (8)$$

which in ref. <sup>49</sup>, Eq. 26 is called the baseline hydrodynamic model. It has the

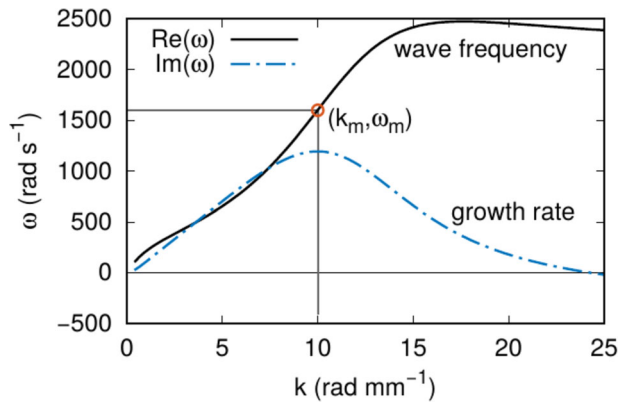


**Fig. 10 Example of the complex dispersion relation  $\omega(k)$ .** Example of the solution of the dispersion relation Eq. (9) for typical conditions in our experiment. The real part gives the wave frequency and the imaginary part the growth rate of the dust density wave for each specific wavenumber  $k$ . For the solution the growth rate is maximal at  $(k_m, \omega_m)$ .

analytical solution

$$\omega = -i \frac{\nu_{dn}}{2} + \sqrt{-\frac{\nu_{dn}^2}{4} + k^2 \nu_{Td}^2 + \frac{\omega_{pd}^2}{1 + \chi_e + \chi_i}} \quad (9)$$

Most of the parameters needed to compute the waves complex frequency  $\omega$  can be determined from the experiment, yet two parameters remain unknown, the ion density  $n_i$  and the ion drift velocity  $v_{i0}$ . Both variables are taken to be the free parameters of the model and the solution can be fitted to pairs  $(\omega_{ex}, k_{ex})$  measured in the experiment.

To calculate the model values  $(\omega_m, k_m)$  (Eq. (9)), we use the drift approximation<sup>50</sup>

$$v_i = \mu E, \quad (10)$$

and the collision frequencies discussed by Tadsen<sup>37</sup>. The particle charge  $q_d$  needs to be determined from its “floating condition”, i.e. the balance of the ion and the electron charging currents (assuming OML approximation):

$$0 = \left( \frac{m_i T_e}{m_e T_i} \right)^{-\frac{1}{2}} \left( 1 - \frac{e\Phi_{fl}}{k_B T_i} \right) - \frac{n_e}{n_i} \exp \left( \frac{e\Phi_{fl}}{k_B T_e} \right). \quad (11)$$

And because electron depletion is important in this case, the CIM model<sup>29</sup> is applied to take it into account:

$$0 = \frac{n_e}{n_i} - 1 - P \frac{e\Phi_{fl}}{k_B T_e}. \quad (12)$$

Figure 1 shows, how the difference between cloud potential and floating potential shrinks due to a lack of electrons for increasing Havnes parameter  $P$ .

This set of equations (9), (11) and (12) can not be meaningfully expanded, but it can be numerically iterated. Starting with a set  $n_{i,s}, v_{i0,s}$  and using the quasi neutrality of the dusty plasma (Eq. (12)), the equations (11) and (12) can be solved and the floating potential  $\Phi_{fl}$  and electron density  $n_e$  are gained. Inserting all results into equation (9) yields the dispersion relation  $\omega(k)$ . An example of such a model dispersion for a pair  $n_i, v_{i0}$  can be seen in Fig. 10.

The imaginary part of the wave frequency  $\text{Im}(\omega(k))$  denotes the stability of the wave. Positive values denote potential for amplitude growth, while negative values indicate dampening. Fluctuations excite the wave, but over a short amount of time the most unstable mode ( $\max(\text{Im}(\omega(k)))$ ) becomes dominant. Therefore the experimentally observed frequency should match the most unstable one (compare Fig. 3) and we take it as the model solution  $(\omega_m, k_m)$ .

From here  $n_i$  and  $v_{i0}$  can be iterated to minimize the deviation

$$D = \sqrt{\left( \frac{\omega_m - \omega_{ex}}{\omega_{ex}} \right)^2 + \left( \frac{k_m - k_{ex}}{k_{ex}} \right)^2}. \quad (13)$$

For the one-dimensional data analysis in the radial direction, the radius of the nanoparticles  $a$  and their density  $n_d$  as well as the local  $\omega$  and  $k$  have to be known from the experiment. The radius of the nanoparticles was measured using Mie polarimetry and the dust density by extinction measurements presented in Methods - Diagnostic for dust density and particle size.

To determine the local  $\omega_{ex}$  and  $k_{ex}$  a video of the wave activity is taken with the high speed (4000 fps) camera C4, see experimental setup (Fig. 8). In a first step the data—taken along the radial direction, at the marked position in the middle of Fig. 2—is Hilbert transformed to estimate the local phase information  $\varphi$  of the

wave. The phase is unwrapped by adding multiples of  $2\pi$ , giving a continuous phase map for every pixel in every frame. Now we use

$$\omega = -\frac{\partial \varphi}{\partial t} \quad (14)$$

$$\mathbf{k} = \nabla \varphi \quad (15)$$

to evaluate the waves properties. Finally the average values of  $\omega$  and  $k$  over all frames are taken (compare Fig. 3b).

The fit at each radial position is completely independent from the other positions. The result of the fitting procedure gives the free parameters in the model  $n_i$  and  $v_{i0}$  as well as the dependent parameters  $E$  and  $q_d$  and all radially resolved plasma parameters which are found in the underlying model equations. In addition to the ion density  $n_i$  and the dust charge  $q_d$  these are the electron density  $n_e$  and the Havnes parameter  $P$ .

As mentioned above, one result of the DDW-D is the ion velocity  $v_{i0}$ . But because the plasma potential  $\Phi_p$  is most interesting considering the confining forces on the nanoparticles, we can determine it by integrating the electric field  $E$ , and the result is shown in Fig. 5c. Yet because the DDW-D cannot provide values for the near dust free region close to the chamber wall, no zero potential is known. Instead, to have a common reference for the different particle sizes, the potential was set zero at  $r = 52$  mm.

It should be mentioned, that the ion and electron temperature can not be determined by our method. Due to the high collision rate with the argon background gas it is assumed that the ions have room temperature  $T_i = 26$  meV. A variation of  $T_e$  between 3 eV and 7 eV for the DDW-D was performed. While the absolute values of e.g. the ion density were differing in the order of 30 percent, the trends and relations described in the results were very much similar. But to apply the DDW as a plasma-technological diagnostic,  $T_e$  must be determined independently. In accordance with the experimental results of Bilik<sup>42</sup>  $T_e$  was chosen to be 5 eV, which is 50% higher than the typical electron temperature of the pristine argon plasma.

## Data availability

The data that support the findings of this study is not publicly available for legal/ethical reasons but available from the corresponding authors on reasonable request.

## Code availability

The Matlab software to analyse the  $\Delta(\Psi)$  curves, to determine the dust density from the extinction measurements and video data, and to analysis the dust density waves are in-house developed. The code is not publicly available for legal/ethical reasons but available from the corresponding authors on reasonable request.

Received: 15 March 2022; Accepted: 27 October 2022;

Published online: 30 November 2022

## References

- Selwyn, G. S., Singh, J. & Bennett, R. S. In situ laser diagnostic studies of plasma-generated particulate contamination. *J. Vac. Sci. Technol. A-Vac. Surf. Films* **7**, 2758–2765 (1989).
- Piel, A. *Plasma Physics - An Introduction to Laboratory, Space, and Fusion Plasmas*, 2nd edn (Springer, 2017).
- Hollenstein, C. The physics and chemistry of dusty plasmas. *Plasma Phys. Controlled Fusion* **42**, R93 (2000).
- Berndt, J. et al. Some aspects of reactive complex plasmas. *Contrib. Plasma Phys.* **49**, 107–133 (2009).
- Hong, S. H. & Winter, J. Size dependence of optical properties and internal structure of plasma grown carbonaceous nanoparticles studied by in situ rayleigh-mie scattering ellipsometry. *J. Appl. Phys.* **100**, 064303 (2006).
- Kortshagen, U. Nonthermal plasma synthesis of nanocrystals: Fundamentals, applications, and future research needs. *Plasma Chem. Plasma Process.* **36**, 73–84 (2016).
- Honda, K. & Kobayashi, R. Fabrication of c-rich a-sic semiconductor nanoparticles having variable optical gaps and particle sizes using high-density plasma in localized area. *Electrochemistry* **88**, 397–406 (2020).
- Cheng, K.-Y., Anthony, R., Kortshagen, U. R. & Holmes, R. J. High-efficiency silicon nanocrystal light-emitting devices. *Nano Lett.* **11**, 1952–1956 (2011).
- Sain, B. & Das, D. Low temperature plasma processing of nc-si/a-sinx:h qd thin films with high carrier mobility and preferred (220) crystal orientation: a promising material for third generation solar cells. *RSC Adv.* **4**, 36929–36939 (2014).



10. Park, S.-W., Jung, J.-S., Kim, K.-S., Kim, K.-H. & Hwang, N.-M. Effect of bias applied to the substrate on the low temperature growth of silicon epitaxial films during rf-pecvd. *Cryst. Growth Des.* **18**, 5816–5823 (2018).
11. Santos, M. et al. Plasma synthesis of carbon-based nanocarriers for linker-free immobilization of bioactive cargo. *ACS Appl. Nano Mater.* **1**, 580–594 (2018).
12. Michael, P. et al. Plasma polymerized nanoparticles effectively deliver dual siRNA and drug therapy in vivo. *Sci. Rep.* **10**, 12836 (2020).
13. Medhi, R., Srinoi, P., Ngo, N., Tran, H.-V. & Lee, R. T. Nanoparticle-based strategies to combat covid-19. *ACS Appl. Nano Mater.* **3**, 8557–8580 (2020).
14. Rabiei, M. et al. Characteristics of sars-cov2 that may be useful for nanoparticle pulmonary drug delivery. *J. Drug Target.* <https://doi.org/10.1080/1061186X.2021.1971236> (2021).
15. De Blecker, K., Bogaerts, A. & Goedheer, W. Modelling of nanoparticle coagulation and transport dynamics in dusty silane discharges. *N. J. Phys.* **8**, 178 (2006).
16. Girshick, S. L. & Chiu, C. P. homogeneous nucleation of particles from the vapor-phase in thermal plasma synthesis. *Plasma Chem. Plasma Process.* **9**, 355–369 (1989).
17. Ravi, L. & Girshick, S. L. Coagulation of nanoparticles in a plasma. *Phys. Rev. E* **79**, 026408 (2009).
18. Bouchoule, A. & Boufendi, L. Particulate formation and dusty plasma behaviour in argon-silane rf discharge. *Plasma Sources Sci. Technol.* **2**, 204 (1993).
19. Kovacevic, E., Berndt, J., Strunskus, T. & Boufendi, L. Size dependent characteristics of plasma synthesized carbonaceous nanoparticles. *J. Appl. Phys.* **112**, 013303 (2012).
20. Agarwal, P. & Girshick, S. L. Sectional modeling of nanoparticle size and charge distributions in dusty plasmas. *Plasma Sources Sci. Technol.* **21**, 055023 (2012).
21. Agarwal, P. & Girshick, S. L. Numerical modeling of an rf argon–silane plasma with dust particle nucleation and growth. *Plasma Chem. Plasma Process.* **34**, 489 (2014).
22. Goertz, C. K. & Morfill, G. E. A model for the formation of spokes in saturn’s ring. *Icarus* **53**, 219–229 (1983).
23. Havnes, O., Morfill, G. E. & Goertz, C. K. Plasma potential and grain charges in a dust cloud embedded in a plasma. *J. Geophys. Res.: Space Phys.* **89**, 10999–11003 (1984).
24. Goertz, C. K. Dusty plasmas in the solar system. *Rev. Geophys.* **27**, 271–292 (1989).
25. Havnes, O., Goertz, C. K., Morfill, G. E., Grün, E. & Ip, W. Dust charges, cloud potential, and instabilities in a dust cloud embedded in a plasma. *J. Geophys. Res.: Space Phys.* **92**, 2281–2287 (1987).
26. Allen, J. E. Probe theory - the orbital motion approach. *Phys. Scr.* **45**, 497–503 (1992).
27. Khrapak, S. A. et al. Particle charge in the bulk of gas discharges. *Phys. Rev. E* **72**, 016406 (2005).
28. Goertz, I., Greiner, F. & Piel, A. Effects of charge depletion in dusty plasmas. *Phys. Plasmas* **18**, 013703 (2011).
29. Melzer, A. & Goree, J. *Low Temperature Plasmas, Fundamentals, Technologies, and Technique*, vol. 1, 2nd edn. chap. 6, 133–134 (Wiley-VCH Verlag, Weinheim, 2008).
30. Barkan, A., D’Angelo, N. & Merlino, R. L. Charging of dust grains in a plasma. *Phys. Rev. Lett.* **73**, 3093–3096 (1994).
31. Bouchoule, A. *Dusty Plasmas: Physics, Chemistry, and Technological Impact in Plasma Processing*, 1st edn. (Wiley, 1999), <https://www.wiley.com/en-us/Dusty+Plasmas%3A+Physics%2C+Chemistry%2C+and+Technological+Impact+in+Plasma+Processing-p-9780471973867>.
32. Hauge, P. & Dill, F. A rotating-compensator fourier ellipsometer. *Opt. Commun.* **14**, 431–437 (1975).
33. Gebauer, G. & Winter, J. In situ nanoparticle diagnostics by multi-wavelength rayleigh-mie scattering ellipsometry. *N. J. Phys.* **5**, 38 (2003).
34. Groth, S., Greiner, F., Tadsen, B. & Piel, A. Kinetic mie ellipsometry to determine the time-resolved particle growth in nanodusty plasmas. *J. Phys. D: Appl. Phys.* **48**, 465203 (2015).
35. Rao, N. N., Shukla, P. K. & Yu, M. Y. Dust-acoustic waves in dusty plasmas. *Planet. Space Sci.* **38**, 543–546 (1990).
36. Rosenberg, M. Ion-dust streaming instability in processing plasmas. *J. Vac. Sci. Technol. A* **14**, 631–633 (1996).
37. Tadsen, B., Greiner, F., Groth, S. & Piel, A. Self-excited dust-acoustic waves in an electron-depleted nanodusty plasma. *Phys. Plasmas* **22**, 113701 (2015).
38. Greiner, F. et al. Diagnostics and characterization of nanodust and nanodusty plasmas. *Eur. Phys. J. D* **72**, 81 (2018).
39. Chutia, B. et al. Spatiotemporal evolution of a self-excited dust density wave in a nanodusty plasma under strong havnes effect. *Phys. Plasmas* **28**, 123702 (2021).
40. Tadsen, B., Greiner, F. & Piel, A. Preparation of magnetized nanodusty plasmas in a radio frequency-driven parallel-plate reactor. *Phys. Plasmas* **21**, 103704 (2014).
41. Klindworth, M., Arp, O. & Piel, A. Langmuir probe system for dusty plasmas under microgravity. *Rev. Sci. Instrum.* **78**, 033502 (2007).
42. Bilik, N., Anthony, R., Merritt, B. A., Aydil, E. S. & Kortshagen, U. R. Langmuir probe measurements of electron energy probability functions in dusty plasmas. *J. Phys. D: Appl. Phys.* **48**, 105204 (2015).
43. Denysenko, I., Ostrikov, K., Yu, M. Y. & Azarenkov, N. A. Behavior of the electron temperature in nonuniform complex plasmas. *Phys. Rev. E* **74**, 036402 (2006).
44. Groth, S., Greiner, F. & Piel, A. Spatio-temporally resolved investigations of layered particle growth in a reactive argon-acetylene plasma. *Plasma Sources Sci. Technol.* **28**, 115016 (2019).
45. Killer, C., Greiner, F., Groth, S., Tadsen, B. & Melzer, A. Long-term spatio-temporal evolution of the dust distribution in dusty argon rf plasmas. *Plasma Sources Sci. Technol.* **25**, 055004 (2016).
46. Buneman, O. Instability, turbulence, and conductivity in current-carrying plasma. *Phys. Rev. Lett.* **1**, 8–9 (1958).
47. Buneman, O. Instability, turbulence, and conductivity in current-carrying plasma. *Phys. Rev. Lett.* **1**, 119 (1958).
48. Kortshagen, U. R. On the use of dust plasma acoustic waves for the diagnostic of nanometer-sized contaminant particles in plasmas. *Appl. Phys. Lett.* **71**, 208–210 (1997).
49. Suranga Ruhunusiri, W. D. & Goree, J. Dispersion relations for the dust-acoustic wave under experimental conditions. *Phys. Plasmas* **21**, 053702 (2014).
50. Frost, L. S. Effect of variable ionic mobility on ambipolar diffusion. *Phys. Rev.* **105**, 354–356 (1957).

## Acknowledgements

We gratefully acknowledge expert advice of Alexander Piel (Kiel University) during development of the dust density wave diagnostic and funding by Deutsche Forschungsgemeinschaft (DFG) of the project GR1608/8-1 “Dusty plasmas with high electron depletion: Investigation of fundamental mechanisms and properties through particle and plasma diagnostic”.

## Author contributions

F.G. supervised and conceived the project and worked out further plans with A.P., O.A., and B.T. A.P. and F.G. carried out the experiments. A.P., O.A., and B.T. developed and enhanced the software of the DDW-analysis. A.P. did the extinction data analysis and prepared the figures. F.G. and A.P. wrote the manuscript. The results and the manuscript were discussed with all authors.

## Funding

Open Access funding enabled and organized by Projekt DEAL.

## Competing interests

The authors declare no competing interests.

## Additional information

**Correspondence** and requests for materials should be addressed to Andreas Petersen or Franko Greiner.

**Reprints and permission information** is available at <http://www.nature.com/reprints>

**Publisher’s note** Springer Nature remains neutral with regard to jurisdictional claims in published maps and institutional affiliations.



**Open Access** This article is licensed under a Creative Commons

Attribution 4.0 International License, which permits use, sharing, adaptation, distribution and reproduction in any medium or format, as long as you give appropriate credit to the original author(s) and the source, provide a link to the Creative Commons license, and indicate if changes were made. The images or other third party material in this article are included in the article’s Creative Commons license, unless indicated otherwise in a credit line to the material. If material is not included in the article’s Creative Commons license and your intended use is not permitted by statutory regulation or exceeds the permitted use, you will need to obtain permission directly from the copyright holder. To view a copy of this license, visit <http://creativecommons.org/licenses/by/4.0/>.

© The Author(s) 2022